

# Quantum-Optimal Object Discrimination in Sub-Diffraction Incoherent Imaging

Michael R Grace<sup>1</sup> and Saikat Guha<sup>1</sup>

<sup>1</sup>*College of Optical Sciences, University of Arizona, Tucson, AZ 85721, USA*

We consider imaging tasks involving discrimination between known objects and investigate the best possible accuracy with which the correct object can be identified. Using the quantum Chernoff bound, we analytically find the ultimate achievable asymptotic error rate for symmetric hypothesis tests between *any* two incoherent 2D objects when the imaging system is dominated by optical diffraction. Furthermore, we show that linear-optical demultiplexing of the spatial modes of the collected light exactly saturates this ultimate performance limit, enabling a quadratic improvement over the asymptotic error rate achieved by direct imaging as the objects become more severely diffraction-limited. We extend our results to identify the quantum limit and optimal measurement for discrimination between an arbitrary number of candidate objects. Our work constitutes a complete theoretical treatment of the ultimate quantitative limits on passive, sub-diffraction, incoherent object discrimination and is readily applicable to a multitude of real-world applications.

Object discrimination is at the heart of decision making in quantitative imaging contexts as diverse as medical diagnostics, extrasolar astronomy, and autonomous sensing. In incoherent imaging contexts involving large standoff distances, small objects, and/or small imaging system apertures, the physical principle of diffraction from a finite aperture degrades the accuracy of discriminating between spatially distinct objects. A classic heuristic criterion, attributed to Rayleigh, holds that candidate objects cannot be successfully discriminated when the distinguishing features of their image-plane signals exhibit length scales smaller than the system point spread function (PSF) width [1]. More quantitatively, discrimination between two or more objects can be cast as a hypothesis test, where the probability of identifying the correct hypothesis depends on the optical detection statistics and the chosen post-processing procedure [2].

A quantum perspective on incoherent imaging has led to the computation of “quantum limits” on imaging performance, most prominently the quantum Crámer-Rao bound (QCRB) for parameter estimation [3]. A quantum limit indicates a fundamental, task-specific performance bound that cannot be exceeded by any measurement scheme allowed by the laws of quantum mechanics, regardless of the presence or absence of quantum phenomena. While diffraction-induced error is unavoidable in quantitative imaging, it was shown that the catastrophic degree of error implied by the Rayleigh criterion is an artifact of the conventional direct imaging measurement at the image plane and that alternative, linear-optical measurements can saturate the QCRB and yield dramatically lower estimation error than direct imaging for many estimation tasks [4–8]. Quantum limits and optimal measurements have also been found for specific hypothesis tests, including one-vs-two point source discrimination [9, 10], which has applications in fluorescence microscopy, and asymmetric exoplanet detection [11]. However, generalizations of these results that can be applied to real-world sub-diffraction object discrimination tasks defined by field-specific experts are not available.

In this Letter, we resolve the general problem of the quantum limits and optimal measurements for sub-diffraction, incoherent object discrimination. For symmetric hypothesis tests between any two incoherent, quasi-monochromatic objects, we 1) find an analytical expression for the quantum limit (i.e., the quantum Chernoff bound) on the asymptotic rate of discrimination error in the sub-diffraction regime  $\gamma \ll 1$ , where  $\gamma$  quantifies the effect of diffraction, 2) show that the asymptotic error rate achievable with direct imaging is strictly worse than this quantum limit by a scaling factor of  $\gamma^2$ , and 3) identify a linear-optical measurement that saturates the quantum limit for any arbitrary pair of incoherent objects. We furthermore describe how our results for binary hypothesis testing can be used to identify quantum limits and optimal measurements for an arbitrary object discrimination task with any number of candidate objects. Interestingly, for both the quantum-optimal measurement and direct imaging, the achievable asymptotic error rates for sub-diffraction object discrimination depend on only the factor  $\gamma$ , the PSF, and the 2D second Cartesian moments of the candidate object models, indicating a generalizable and quantifiable tradeoff between imaging geometry, object similarity, and discrimination performance. As our results are not limited to particular object or aperture models, they can be readily applied to any sub-diffraction object discrimination setting.

Let  $H_j$  denote a hypothesis corresponding to one of multiple candidate objects. Under  $H_j$ , we use the mixed quantum state  $\rho_j$  to describe the quasi-monochromatic optical field collected by the system aperture in a single temporal mode. Typical incoherent sources (in fluorescence microscopy, astronomy, etc.) exhibit sufficiently small photon fluxes that multi-photon detection events within the coherent time window of a given temporal mode are vanishingly rare [12]. Under this weak-source model, the multi-spatial-mode state  $\rho_j$  can be approximated by the first two terms in the expansion [4]

$$\rho_j = (1 - \epsilon)|0\rangle\langle 0| + \epsilon\rho_j + O(\epsilon^2), \quad (1)$$

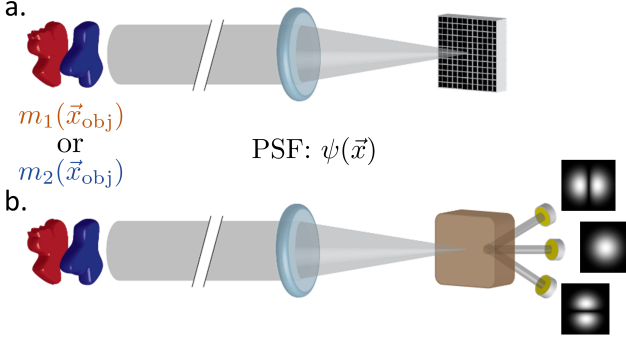


FIG. 1. Discrimination of objects  $m_1(\vec{x}_{\text{obj}})$  and  $m_2(\vec{x}_{\text{obj}})$ . a. Direct imaging using a focal plane array. b. TriSPADE measurement using an image-plane spatial mode sorting module and three intensity-resolving detectors. For a Gaussian PSF  $\psi(\vec{x})$ , the measured spatial modes are shown at right.

where  $\epsilon$  is the average photon flux per temporal mode,  $|0\rangle\langle 0|$  is the quantum vacuum state, and the state  $\rho_j$  is conditioned on the detection of a single photon and contains all of the spatial information about the  $j^{\text{th}}$  object. Since  $\rho_j$  is restricted to single-photon (unary) excitation, its infinite-dimensional spatial mode distribution lives in a  $L^2$  space that can be mapped onto a Hilbert space  $\mathcal{H}$ . Assuming static objects, the information-bearing optical field collected over  $M$  temporal modes is described by the tensor product  $\rho_j^{\otimes n}$ , where  $n$  is the Poisson-distributed number of detected photons with mean  $N = \epsilon M$  [12].

A spatial description of the quasi-monochromatic, incoherent object under hypothesis  $H_j$  is given by the 2D normalized radiant exitance profile  $m_j(\vec{x}_{\text{obj}}) > 0$ , where the position vector  $\vec{x}_{\text{obj}} = \vec{x}/\mu$  at the object plane is related to the image-plane position vector  $\vec{x} = \{x, y\}$  by the transverse magnification  $\mu$ . We write the single-photon quantum state on  $\mathcal{H}$  that models the incoherent radiation emitted from this object and collected by a system aperture with a 2D coherent PSF  $\psi(\vec{x})$  as [2, 13]

$$\rho_j = \int_{-\infty}^{\infty} \int_{-\infty}^{\infty} \frac{1}{\mu^2} m_j\left(\frac{\vec{x}}{\mu}\right) |\psi_{\vec{x}}\rangle\langle\psi_{\vec{x}}| d^2\vec{x}, \quad (2)$$

where the pure state  $|\psi_{\vec{x}}\rangle = \int_{-\infty}^{\infty} \int_{-\infty}^{\infty} \psi(\vec{a} - \vec{x}) |\vec{a}\rangle d^2\vec{a}$  encodes the effect of the aperture and  $|\vec{x}\rangle = a^\dagger(\vec{x})|0\rangle$  is a single-photon position eigenket [4]. In a basis of generalized eigenvectors  $|\phi_m\rangle = \int_{-\infty}^{\infty} \int_{-\infty}^{\infty} \phi_m(\vec{x}) |\vec{x}\rangle d^2\vec{x}$ , where the 2D functions  $\phi_m(\vec{x})$  satisfy  $\langle\phi_m|\phi_n\rangle = \delta_{m,n}$ , we define  $c_{m,n}(\vec{x}) = \langle\phi_m|\psi_{\vec{x}}\rangle\langle\psi_{\vec{x}}|\phi_n\rangle$  and write the state

$$\rho_j = \sum_{m,n=0}^{\infty} d_{j,m,n} |\phi_m\rangle\langle\phi_n| \quad (3)$$

$$d_{j,m,n} = \int_{-\infty}^{\infty} \int_{-\infty}^{\infty} \frac{1}{\mu^2} m_j\left(\frac{\vec{x}}{\mu}\right) c_{m,n}(\vec{x}) d^2\vec{x}. \quad (4)$$

Consider a binary hypothesis test between incoherent objects  $m_1(\vec{x}_{\text{obj}})$  and  $m_2(\vec{x}_{\text{obj}})$  (Fig. 1) with prior probabilities  $\pi_1 = \pi_2 = 1/2$ . A receiver at the image plane

is tasked to make a decision  $Z \in [1, 2]$  on which candidate object is present based on  $n$  identical copies of the single-photon quantum state  $\rho_1$  or  $\rho_2$ . The decision will be made by performing measurements on the collected light and, subsequently, applying a pre-determined decision rule on the obtained measurement outcomes  $\{z\}$ . If  $P_n(Z = j'|H_j)$  is the conditional probability of guessing  $H_{j'}$  under true hypothesis  $H_j$ , the average error probability  $P_{\text{err},n} = (1/2)[P_n(Z = 1|H_2) + P_n(Z = 2|H_1)]$  is a symmetric performance measure for a particular measurement-decision rule scheme. In the limit of high copy number ( $n \gg 1$ ), the average error probability can be asymptotically expressed as  $P_{\text{err},n} = (1/2)e^{-\xi n}$ , where the error exponent  $\xi > 0$  quantifies how efficiently each additional observation drives down the average error [14].

Given a chosen measurement, the Chernoff bound sets the best possible error rate over all decision rules for symmetric hypothesis tests [14]. The Chernoff exponent (CE)  $\xi_C \geq \xi$  is a statistical quantity computed from measurement outcome probabilities  $P(z|\rho_j)$ ; for a measurement applied individually on each copy of the state  $\rho_1$  or  $\rho_2$ ,

$$\xi_C = -\log \left[ \min_{0 \leq s \leq 1} \sum_{z \in \mathcal{Z}} P(z|\rho_1)^s P(z|\rho_2)^{1-s} \right]. \quad (5)$$

The most general quantum description of a physically realizable measurement is a positive operator-valued measure (POVM), which consists of a set of positive semi-definite operators  $\{\Pi_z\}_{z \in \mathcal{Z}}$  on  $\mathcal{H}$  that correspond to measurement outcomes  $\{z\}$  on an outcome space  $\mathcal{Z}$  and resolve the identity operator as  $\sum_{z \in \mathcal{Z}} \Pi_z = \mathcal{I}$  [15]. The probability of obtaining outcome  $z$  from a measurement of the state  $\rho_j$  is then given by  $P(z|\rho_j) = \text{Tr}(\rho_j \Pi_z)$ . To compute the quantum limit for binary object discrimination, we use the quantum Chernoff bound, where [16, 17]

$$\xi_Q = -\log \left[ \min_{0 \leq s \leq 1} \text{Tr}(\rho_1^s \rho_2^{1-s}) \right] \quad (6)$$

is the quantum Chernoff exponent (QCE). The QCE automatically optimizes  $\xi_C$  over all POVMs on  $\mathcal{H}^{\otimes n}$  [18], setting an achievable ultimate upper bound  $\xi_Q \geq \xi_C \geq \xi$ . A measurement whose CE saturates the bound ( $\xi_C = \xi_Q$ ) is a “quantum-optimal” measurement for the given hypothesis test. Conversely, a gap with respect to the quantum limit ( $\xi_C < \xi_Q$ ) indicates a fundamental sub-optimality in the chosen measurement that cannot be remedied by data post-processing.

We first consider the task of discriminating an arbitrary 2D incoherent object from a point source, an example application being exoplanet detection [11]. The candidate objects in this case are a point source at position  $\vec{x}_{1,\text{obj}} = \vec{x}_1/\mu$ , described by a pure state  $\rho_1 = |\psi_{\vec{x}_1}\rangle\langle\psi_{\vec{x}_1}|$ , and a second object  $m_2(\vec{x}_{\text{obj}})$  with state  $\rho_2$  (Eq. 2). Assuming a shift invariant imaging system and paraxial optics [2], the statistical distance between the two objects will not be changed by a global coordinate shift such

that  $\rho_1 = |\psi_{\vec{0}}\rangle\langle\psi_{\vec{0}}|$ , where  $\vec{0}$  indicates the origin on a 2D Cartesian coordinate system. The shifted second object is then  $m_2(\vec{x}_{\text{obj}} - \vec{x}_{1,\text{obj}})$ . Since the QCE for a binary hypothesis test where  $H_1$  indicates a pure state is exactly given by  $\xi_Q = -\log[\langle\psi_{\vec{0}}|\rho_2|\psi_{\vec{0}}\rangle]$  [19], the QCE is

$$\xi_Q = -\log\left[\int_{-\infty}^{\infty}\int_{-\infty}^{\infty}\frac{1}{\mu^2}m_2\left(\frac{\vec{x}-\vec{x}_1}{\mu}\right)|\Gamma(\vec{x})|^2d^2\vec{x}\right] \quad (7)$$

for any arbitrary  $m_2(\vec{x}_{\text{obj}})$ , where  $\Gamma(\vec{x}) = \langle\psi_{\vec{0}}|\psi_{\vec{x}}\rangle$  is the 2D autocorrelation function of the PSF. Additionally, for pure-vs-mixed state hypothesis tests, the projective measurement with POVM elements  $\Pi_0 = |\psi_{\vec{0}}\rangle\langle\psi_{\vec{0}}|$  and  $\Pi_1 = \mathcal{I} - |\psi_{\vec{0}}\rangle\langle\psi_{\vec{0}}|$  is known to be quantum-optimal [19]. In the incoherent imaging context, this measurement can be implemented with a 2D binary spatial mode demultiplexing (BSPADE) device [4, 20, 21] that passively couples the spatial mode matched to the PSF to one intensity detector and all other light to a second intensity detector.

A special case of these preliminary results is discrimination between a single point source, modeled by the state  $\rho_1 = |\psi_{\vec{0}}\rangle\langle\psi_{\vec{0}}|$ , and two point sources, modeled by  $\rho_2 = (1/2)(|\psi_{\{-d/2,0\}}\rangle\langle\psi_{\{-d/2,0\}}| + |\psi_{\{d/2,0\}}\rangle\langle\psi_{\{d/2,0\}}|)$ , where  $d$  is the spatial separation between the two point sources along the  $x$  axis. Using a 2D Gaussian PSF  $\psi(\vec{x}) = (2\pi\sigma^2)^{-2} \exp(-(x^2+y^2)/4\sigma^2)$ , our result in Eq. 7 with  $\mu = 1$  and  $\sigma = 1$  reproduces the reported QCE of  $\xi_Q = d^2/16$  [9], which is equaled by the CE of the quantum-optimal 2D BSPADE measurement. For comparison, typical receivers for incoherent imaging use the direct imaging measurement (Fig. 1a.), which consists of an image-plane detector array (e.g., a camera sensor) that records arrival positions of incident photons. Idealized 2D direct imaging (i.e., using a 2D detector array with infinite spatial extent and spatial bandwidth, unity fill factor, and unity quantum efficiency) can be described as a continuously sampled projective measurement with differential POVM elements  $d\Pi_{\vec{x}} = |\vec{x}\rangle\langle\vec{x}|d^2\vec{x}$ , where  $\int_{\mathbb{R}^2} d\Pi_{\vec{x}} = \mathcal{I}$ . Ref. [9] found that the CE for ideal direct imaging is  $\xi_{\text{C,Direct}} \approx d^4/256$  to lowest order in  $d \ll 1$ , indicating a quadratic scaling gap in the achievable error exponent compared with the quantum limit as the point-source separation under  $H_2$  is made small.

We now generalize the imaging task to arbitrary, intensity-normalized objects  $m_1(\vec{x}_{\text{obj}})$  and  $m_2(\vec{x}_{\text{obj}})$ . In the following, we fix the 2D centroids of both objects to a known origin (i.e.,  $\int_{-\infty}^{\infty}\int_{-\infty}^{\infty}x_{\text{obj}}m_j(\vec{x}_{\text{obj}})d^2\vec{x}_{\text{obj}} = 0$  and  $\int_{-\infty}^{\infty}\int_{-\infty}^{\infty}y_{\text{obj}}m_j(\vec{x}_{\text{obj}})d^2\vec{x}_{\text{obj}} = 0$ ). These constraints do not betray any information about which of the two candidates is present but rather cast the imaging task as the identification of an object whose centroid is located *a priori*, either because of prior knowledge about the scene or via a suitable preliminary measurement [22–24]. We also assume that the PSF  $\psi(\vec{x})$  is everywhere an even function in  $x$  and  $y$ , for which the common assumption of a circularly symmetric system aperture is sufficient. In

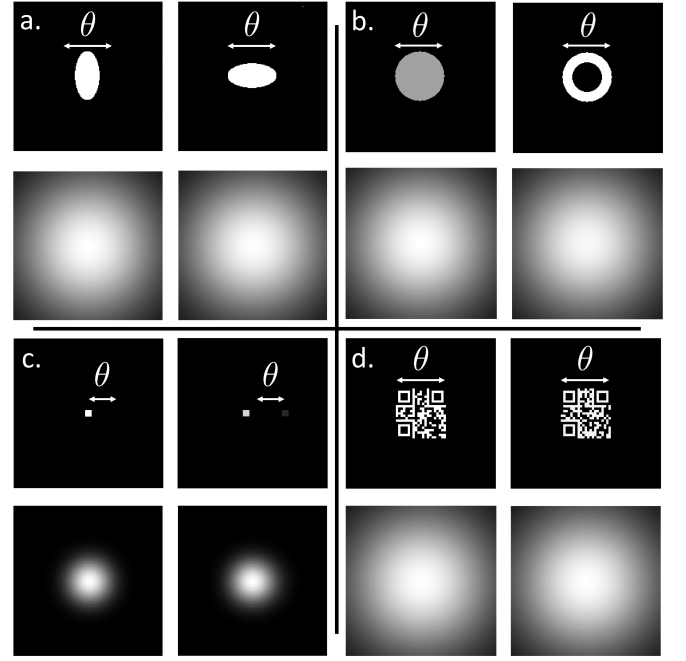


FIG. 2. Examples of normalized incoherent object pairs for binary hypothesis testing: a. vertical vs. horizontal ellipses, b. filled vs. hollow pores, c. exoplanet detection, and d. binary QR code reading. For each example, the upper two images show the ground truth objects and the lower two images show the PSF-convolved image-plane intensity profiles at  $\gamma = 1$ .

Fig. 2 we show four simplified object pairs demonstrating example applications for this imaging scenario. We introduce the parameter  $\gamma = \mu\theta/\sigma$  to geometrically relate the scene to the diffractive imaging system, where  $\theta > 0$  and  $\sigma > 0$  quantify the spatial extent of the object(s) and the PSF width, respectively. These two loosely defined parameters can be specified such that the condition  $\gamma = 1$  reflects a particular (heuristic) criterion for object resolvability; in keeping with recent literature, we use the term “sub-Rayleigh” for the regime where  $\gamma < 1$ . Practically, the ratio  $\gamma$  will decrease if the object size is reduced, if the distance to the object is increased, or if the system aperture diameter is decreased [2]. Furthermore, we argue in the Supplementary Material that the quantities  $\tilde{m}_j(\vec{x}_{\text{obj}}) = \theta^2 m_j(\theta\vec{x}_{\text{obj}})$ ,  $\psi(\vec{x}) = \sigma\psi(\sigma\vec{x})$ , and  $\tilde{\Gamma}(\vec{x}) = \Gamma(\sigma\vec{x})$  are appropriately normalized, non-dimensionalized representations of the object(s), the coherent PSF, and the PSF autocorrelation function with the effect of the spatial diffraction ratio  $\gamma$  removed.

We outline our derivation of the QCE for hypothesis tests between any two sub-Rayleigh incoherent objects here; see the Supplementary Material for details. To represent the quantum states  $\rho_1$  and  $\rho_2$  (Eq. 3), we select as our basis vectors  $|\phi_m\rangle$  the PSF-adapted (PAD) basis, an orthonormal basis on  $\mathcal{H}$  beginning with the centered PSF vector  $|\phi_0\rangle = |\psi_{\vec{0}}\rangle$  [25–27]. The remaining PAD ba-

$m$	0	1	2	3	4	5
$k_m$	0	1	0	2	1	0
$l_m$	0	0	1	0	1	2

TABLE I. Indexing convention used for the first six PAD basis vectors (indexed by  $m$ ) and their relationships with the  $x$  and  $y$  derivatives of the PSF (indexed by  $k_m$  and  $l_m$ ).

sis vectors  $|\tilde{\phi}_m\rangle = \int_{-\infty}^{\infty} \int_{-\infty}^{\infty} \tilde{\phi}_m(\vec{x})|\vec{x}\rangle d^2\vec{x}$  are constructed by performing a Gram-Schmidt orthogonalization of vectors  $|\partial_{x^{k_m}y^{l_m}}\tilde{\psi}_{\vec{\Omega}}\rangle$  corresponding to 2D Cartesian derivatives of the non-dimensionalized PSF, where the index  $m$  is mapped to the two indices  $k_m, l_m$  according to Table I. For example, in the case of a Gaussian PSF, the PAD basis functions  $\tilde{\phi}_m(\vec{x})$  are given by the 2D Hermite-Gauss polynomials [26]. In this basis, we Taylor expand  $m_1(\vec{x}_{\text{obj}})$  and  $m_2(\vec{x}_{\text{obj}})$  in the Fourier domain to find

$$d_{j,m,n} = \sum_{k,l=0}^{\infty} (-1)^{p_m+p_n+k+l} \frac{\gamma^{k+l}}{k!l!} \times m_{j,x_{\text{obj}}^k y_{\text{obj}}^l} \left[ \frac{\partial^{k+l} \tilde{c}_{m,n}(\vec{x})}{\partial x^k \partial y^l} \right]_{\vec{x}=\vec{\Omega}}, \quad (8)$$

where  $p_m = k_m + l_m$ ,  $\tilde{c}_{m,n}(\vec{x}) = c_{m,n}(\sigma\vec{x})$ , and where

$$m_{j,x_{\text{obj}}^k y_{\text{obj}}^l} = \int_{-\infty}^{\infty} \int_{-\infty}^{\infty} x_{\text{obj}}^k y_{\text{obj}}^l \tilde{m}_j(\vec{x}_{\text{obj}}) d^2\vec{x}_{\text{obj}}, \quad (9)$$

give the spatial moments in  $x_{\text{obj}}$  and  $y_{\text{obj}}$  of the non-dimensionalized object models. Eq. 8 is a general expression, expressed as a series in powers of  $\gamma$ , for the PAD basis density matrix elements of any incoherent object.

The PAD basis is a convenient choice because the quantum states  $\rho_j$  corresponding to sub-Rayleigh objects only contain appreciable excitation probability amplitudes in a small number of lowest-order PAD modes [5]. Therefore,  $\rho_1$  and  $\rho_2$  can be truncated in the PAD basis to finite-dimensional density matrix representations, and we analytically find all of the non-zero density matrix elements  $d_{j,m,n}$  to second order in  $\gamma$ . Finally, we use our work on perturbative expansions for quantum information theoretic measures [28] to write the QCE as [29]

$$\begin{aligned} \xi_Q = \max_{0 \leq s \leq 1} & \left[ s(m_{1,x_{\text{obj}}^2} \Gamma_{x^2} + m_{1,y_{\text{obj}}^2} \Gamma_{y^2}) \right. \\ & + (1-s)(m_{2,x_{\text{obj}}^2} \Gamma_{x^2} + m_{2,y_{\text{obj}}^2} \Gamma_{y^2}) \\ & - m_{1,x_{\text{obj}}}^s m_{2,x_{\text{obj}}}^{1-s} \Gamma_{x^2} - m_{1,y_{\text{obj}}}^s m_{2,y_{\text{obj}}}^{1-s} \Gamma_{y^2} \Big] \gamma^2 \\ & + O(\gamma^3), \end{aligned} \quad (10)$$

where the quantities

$$\Gamma_{x^k y^l} = - \left[ \text{Re} \left( \frac{\partial^{k+l} \tilde{\Gamma}(\vec{x})}{\partial x^k \partial y^l} \right) \right]_{\vec{x}=\vec{\Omega}} \quad (11)$$

are derivatives of the non-dimensionalized PSF autocorrelation function. Eq. 10 is the primary result of our work and can be used to find the ultimate limit on the asymptotic error exponent for binary hypothesis tests between *any* two incoherent objects in the sub-Rayleigh limit ( $\gamma \ll 1$ ). It is instructive to compare the QCE against the CE for direct imaging, which in the same regime is given by (see Supplementary Material)

$$\xi_{\text{C,Direct}} = \frac{\mathcal{K}}{32} \gamma^4 + O(\gamma^5), \quad (12)$$

where

$$\begin{aligned} \mathcal{K} = \int_{-\infty}^{\infty} \int_{-\infty}^{\infty} & \left| \tilde{\psi}(\vec{x}) \right|^{-2} \left( (m_{1,x_{\text{obj}}^2} - m_{2,x_{\text{obj}}^2}) \psi_{x^2}(\vec{x}) \right. \\ & \left. + (m_{1,y_{\text{obj}}^2} - m_{2,y_{\text{obj}}^2}) \psi_{y^2}(\vec{x}) \right)^2 d^2\vec{x} \end{aligned} \quad (13)$$

and where the quantity  $\psi_{x^k y^l}(\vec{x}) = \partial^{k+l} |\tilde{\psi}(\vec{x})|^2 / \partial x^k \partial y^l$  represents derivatives of the incoherent PSF. Eqs. 10 and 12 prove that, for sub-Rayleigh binary object discrimination, direct imaging is strictly sub-optimal by a quadratic factor in the diffraction ratio  $\gamma$  (i.e.,  $O(\gamma^4)$  vs  $O(\gamma^2)$ ) [30].

Having found the quantum limit, we now identify a quantum-optimal measurement for arbitrary binary sub-diffraction object discrimination. The PAD-basis projectors  $\Pi_0 = |\phi_0\rangle\langle\phi_0|$ ,  $\Pi_1 = |\phi_1\rangle\langle\phi_1|$ , and  $\Pi_2 = |\phi_2\rangle\langle\phi_2|$  can be implemented with linear optics and photodetectors [20, 21] and map to a “TriSPADE” measurement (Fig. 1b.) that sorts the collected light between the PSF-matched spatial mode as well as the first-order PAD-basis modes in two perpendicular transverse dimensions. We show in the Supplementary Material that in the sub-Rayleigh limit, these three projectors losslessly capture the collected optical field, and the resulting CE ( $\xi_{\text{TriSPADE}}$ ) saturates the QCE in the sub-Rayleigh limit. TriSPADE does not depend on the candidate object models and is thus a quantum-optimal structured receiver for arbitrary binary sub-Rayleigh object discrimination.

To demonstrate our theory, in Fig. 3 we specify a 2D Gaussian PSF and numerically evaluate  $\xi_Q$ ,  $\xi_{\text{C,TriSPADE}}$ , and  $\xi_{\text{C,Direct}}$  for the object discrimination tasks displayed in Fig. 2. We define  $\theta$  to be the full spatial extent of the objects, such that the condition  $\gamma = 1$  is a Rayleigh-like criterion for the extended objects. In each case, the numerically evaluated (Q)CEs agree with our analytical results in the sub-Rayleigh limit. In particular, the lowest-order scaling behavior of the QCE (Eq. 10) is an excellent approximation for both the true QCE and the TriSPADE CE throughout the sub-Rayleigh regime ( $\gamma < 1$ ), and the numerical results clearly exhibit the expected  $\gamma^4$  vs  $\gamma^2$  scaling gap. Our results are also robust to optical misalignment; using a mode sorter that is misaligned from the mutual object centroid, the  $O(\gamma^2)$  scaling gap between  $\xi_{\text{C,Direct}}$  and  $\xi_{\text{C,TriSPADE}}$  is retained (Fig. 3c). These results suggest that a large advantage over direct imaging is achievable for a wide range of sub-diffraction hypothesis tests.

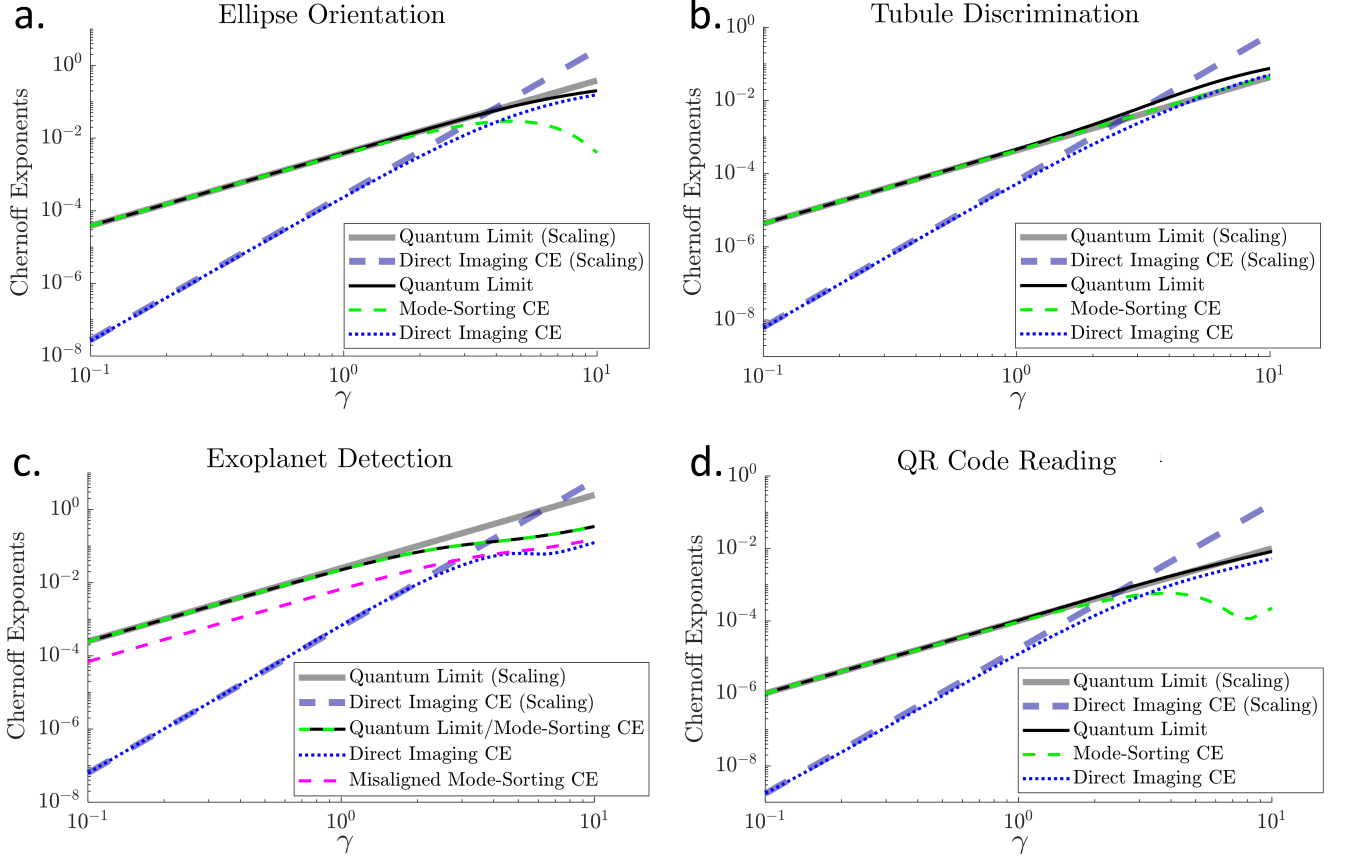


FIG. 3. Upper bounds on the asymptotic error exponents for the imaging tasks shown in Fig. 2 with a 2D Gaussian PSF. Thick lines: analytical lowest-order scaling results for  $\gamma \ll 1$  for  $\xi_Q$  (solid) and  $\xi_{C, \text{Direct}}$  (dashed). Thin lines: numerical results for  $\xi_Q$  (solid),  $\xi_{C, \text{Direct}}$  (dotted), and  $\xi_{C, \text{TriSPADE}}$  (dashed). A misalignment of  $\theta/10$  is used for the misaligned TriSPADE CE in c.

We can further extend our results to imaging tasks involving more than two candidate objects, such as a database of QR codes (Fig. 2d.). For hypothesis testing between multiple quantum states, the quantum limit is given by the minimum of the QCEs computed on each pair of states [31]. Thus, minimizing over all pairwise QCEs among the candidate incoherent objects gives the ultimate achievable upper bound on the asymptotic error exponent associated with failing to choose the correct object. In the example of identifying a QR code from a database, the ultimate bound will be determined by the hardest-to-discriminate pair of QR codes, which, according to Eq. 10, depends solely on the non-dimensionalized 2D second moments of the respective QR code models. This naturally leads to the concept of a “distance” of a set of objects based on relative second moments that, along with the diffraction ratio  $\gamma$ , gives rise to a tradeoff against the ultimate performance of sub-Rayleigh multiple object discrimination. Finally, the objects’ quantum states (Eq. 2) define a prescriptive measurement scheme that achieves the ultimate quantum limit [31].

In conclusion, our results indicate the potential for realizable optical receivers that could dramatically im-

prove object discrimination performance for real-world sub-diffraction imaging needs. Such solutions could tremendously benefit autonomous inference in biological, astronomical, and terrestrial imaging via our TriSPADE receiver design and/or new methods that approach the sub-Rayleigh quantum limit. For example, a four-element, 2D inversion-interferometric measurement (SLIVER) [21, 32] that sorts the even-odd transverse parity of the collected light will also be quantum-optimal for sub-Rayleigh binary object discrimination and may be easier to implement for some applications. In addition to spurring the development of quantum-optimal imaging schemes, the QCE is an ultimate bound that precludes superior discrimination accuracy for a given imaging task, meaning that no combination of optical pre-processing and/or digital post-processing can produce an error exponent exceeding Eq. 10. It also follows that system imperfections, such as optical losses, detector crosstalk/noise, or spatial misalignment will always result in inferior discrimination accuracy compared to our calculated quantum limit. Thus, our results will aid in ruling out quantitative regimes of discrimination capability in the development of future imaging systems.

This research was supported by the DARPA IAMBIC Program under contract number HR00112090128. The views, opinions and/or findings expressed are those of the authors and should not be interpreted as representing the official views or policies of the Department of Defense or the U.S. Government.

- 
- [1] L. Rayleigh, Investigations in optics, with special reference to the spectroscope, *Philos. Magazine* **5**, 261 (1879).
  - [2] J. W. Goodman, *Introduction to Fourier Optics*, 3rd ed. (Roberts and Company, Englewood, CO, USA, 2005).
  - [3] M. Tsang, Resolving starlight: a quantum perspective, *Contemporary Physics* **60**, 279 (2020).
  - [4] M. Tsang, R. Nair, and X. M. Lu, Quantum theory of superresolution for two incoherent optical point sources, *Physical Review X* **6**, 031033 (2016).
  - [5] Z. Dutton, R. Kerviche, A. Ashok, and S. Guha, Attaining the quantum limit of superresolution in imaging an object's length via predetection spatial-mode sorting, *Physical Review A* **99**, 033847 (2019).
  - [6] M. Tsang, Quantum Limit to Subdiffraction Incoherent Optical Imaging, *Physical Review A* **99**, 012305 (2019).
  - [7] S. Zhou and L. Jiang, A modern description of Rayleigh's criterion, *Physical Review A* **99**, 013808 (2019).
  - [8] C. Lupo, Z. Huang, and P. Kok, Quantum Limits to Incoherent Imaging are Achieved by Linear Interferometry, *Physical Review Letters* **124**, 080503 (2020).
  - [9] X. M. Lu, H. Krovi, R. Nair, S. Guha, and J. H. Shapiro, Quantum-optimal detection of one-versus-two incoherent optical sources with arbitrary separation, *npj Quantum Information* **64** (2018).
  - [10] H. Zhang, S. Kumar, and Y. Huang, A Super-resolution Optical Classifier with High Photon Efficiency, *Optics Letters* **45**, 10.1364/ol.401614 (2020).
  - [11] Z. Huang and C. Lupo, Quantum hypothesis testing for exoplanet detection, arXiv:2106.00488 (2021).
  - [12] L. Mandel, Fluctuations of Photon Beams: The Distribution of the Photo-Electrons, *Proceedings of the Physical Society* **74** (1959).
  - [13] M. Tsang, Subdiffraction incoherent optical imaging via spatial-mode demultiplexing, *New Journal of Physics* **19**, 10.1088 (2017).
  - [14] H. L. Van Trees and K. Bell, *Detection Estimation and Modulation Theory, Part I: Detection, Estimation, and Filtering Theory*, 2nd ed. (John Wiley & Sons, Hoboken, New Jersey, 2013).
  - [15] C. W. Helstrom, *Quantum Detection and Estimation Theory* (Academic Press, Inc., New York, 1976).
  - [16] K. M. Audenaert, J. Calsamiglia, R. Muñoz-Tapia, E. Bagan, L. Masanes, A. Acín, and F. Verstraete, Discriminating states: The quantum Chernoff bound, *Physical Review Letters* **98**, 160501 (2007).
  - [17] M. Nussbaum and A. Szkola, The Chernoff lower bound for symmetric quantum hypothesis testing, *Annals of Statistics* **37**, 10.1214/08-AOS593 (2009).
  - [18] The quantum Chernoff bound optimizes over all POVMs including measurements that act collectively on multiple copies of the state  $\rho_j$ . Our results show that individual measurements on each copy of  $\rho_j$  (i.e., on each photon) is sufficient to saturate the quantum Chernoff bound.
  - [19] V. Kargin, On the chernoff bound for efficiency of quantum hypothesis testing, *Annals of Statistics* **33**, 10.1214/009053604000001219 (2005).
  - [20] P. Boucher, C. Fabre, G. Labroille, and N. Treps, Spatial optical mode demultiplexing as a practical tool for optimal transverse distance estimation, *Optica* **7** (2020).
  - [21] S. Z. Ang, R. Nair, and M. Tsang, Quantum limit for two-dimensional resolution of two incoherent optical point sources, *Physical Review A* **95**, 063847 (2017).
  - [22] A. Sajjad, M. R. Grace, Q. Zhuang, and S. Guha, Attaining quantum limited precision of localizing an object in passive imaging, arXiv:2102.02228 (2021).
  - [23] M. R. Grace, Z. Dutton, A. Ashok, and S. Guha, Approaching quantum-limited imaging resolution without prior knowledge of the object location, *Journal of the Optical Society of America A* **37**, 1288 (2020).
  - [24] J. O. de Almeida, C. Hirche, M. Lewenstein, and M. Skotiniotis, Discrimination and estimation of incoherent sources under misalignment J., *Physical Review A* **103**, 022406 (2021).
  - [25] R. Kerviche, S. Guha, and A. Ashok, Fundamental limit of resolving two point sources limited by an arbitrary point spread function, *IEEE International Symposium on Information Theory - Proceedings* 10.1109/ISIT.2017.8006566 (2017).
  - [26] J. Řeháček, M. Paúr, B. Stoklasa, Z. Hradil, and L. L. Sánchez-Soto, Optimal measurements for resolution beyond the Rayleigh limit, *Optics Letters* **42**, 10.1364/OL.42.000231 (2017).
  - [27] M. Tsang, Subdiffraction incoherent optical imaging via spatial-mode demultiplexing: Semiclassical treatment, *Physical Review A* **97**, 023830 (2018).
  - [28] M. R. Grace and S. Guha, Perturbation Theory for Quantum Information, arXiv:2106.05533 (2021).
  - [29] While we only addresses symmetric hypothesis tests here, our perturbation theory for quantum information [28] will enable generalized results on asymmetric object discrimination via the quantum Stein lemma in future work.
  - [30] In the Supplementary Material we discuss two caveats to these scaling results. First, if the two objects have identical second moments in  $x_{\text{obj}}$  and  $y_{\text{obj}}$  such that the lowest-order moment in which the two objects differ is of order  $\kappa > 2$ , we find that  $\xi_{\text{C,Direct}} = O(\gamma^{2\kappa})$  and  $\xi_{\text{Q}} = O(\gamma^\kappa)$ , resulting in a larger scaling gap of  $O(\gamma^\kappa)$ . However, if the object models have different first moments, i.e., different 2D centroids, then  $\xi_{\text{C,Direct}} = O(\gamma^2)$  and  $\xi_{\text{Q}} = O(\gamma^2)$ , and the scaling gap vanishes. These caveats indicate that the relative performance gap generally tends to increase with greater absolute difficulty of the discrimination task.
  - [31] K. Li, Discriminating quantum states: The multiple chernoff distance, *Annals of Statistics* **44**, 10.1214/16-AOS1436 (2016).
  - [32] R. Nair and M. Tsang, Interferometric superlocalization of two incoherent optical point sources, *Optics Express* **24**, 10.1364/oe.24.003684 (2016).
  - [33] M. Paúr, B. Stoklasa, D. Koutný, J. Řeháček, Z. Hradil, J. Grover, A. Krzic, and L. L. Sánchez-Soto, Reading out Fisher information from the zeros of the point spread function, *Optics Letters* **44** (2019).

## SUPPLEMENTARY MATERIAL

### Non-Dimensionalized Quantities

We first justify the definitions for the non-dimensionalized quantities  $\tilde{m}_j(\vec{x}_{\text{obj}})$ ,  $\tilde{\psi}(\vec{x})$  and  $\tilde{\Gamma}(\vec{x})$ . We seek normalization factors  $a$  and  $b$  such that  $\tilde{m}_j(\vec{x}_{\text{obj}}) = am_j(\theta\vec{x}_{\text{obj}})$  and  $\tilde{\psi}(\vec{x}) = b\psi(\sigma\vec{x})$  satisfy the normalization conditions  $1 = \int_{-\infty}^{\infty} \int_{-\infty}^{\infty} \tilde{m}_j(\vec{x}_{\text{obj}}) d^2\vec{x}_{\text{obj}}$  and  $1 = \int_{-\infty}^{\infty} \int_{-\infty}^{\infty} \tilde{\psi}^*(\vec{x})\tilde{\psi}(\vec{x}) d^2\vec{x}$ . Making the coordinate transformations  $\vec{x}'_{\text{obj}} = \theta\vec{x}_{\text{obj}}$  and  $\vec{x}' = \sigma\vec{x}$ , we have

$$\begin{aligned} 1 &= \frac{a}{\theta^2} \int_{-\infty}^{\infty} \int_{-\infty}^{\infty} m_j(\vec{x}'_{\text{obj}}) d^2\vec{x}'_{\text{obj}} \\ 1 &= \frac{|b|^2}{\sigma^2} \int_{-\infty}^{\infty} \int_{-\infty}^{\infty} \psi^*(\vec{x}')\psi(\vec{x}') d^2\vec{x}'. \end{aligned} \quad (14)$$

Since each of the integrals in Eq. (14) is equal to unity, we confirm the normalizations  $a = \theta^2$  and  $b = \sigma$ . Using the definition  $\tilde{\Gamma}(\vec{x}) = \Gamma(\sigma\vec{x})$ , we then have

$$\begin{aligned} \tilde{\Gamma}(\vec{x}) &= \int_{-\infty}^{\infty} \int_{-\infty}^{\infty} \psi^*(\vec{a})\psi(\vec{a} - \sigma\vec{x}) d^2\vec{a} \\ &= \int_{-\infty}^{\infty} \int_{-\infty}^{\infty} \sigma^2 \psi^*(\sigma\vec{a})\psi(\sigma\vec{a} - \sigma\vec{x}) d^2\vec{a} \\ &= \int_{-\infty}^{\infty} \int_{-\infty}^{\infty} \tilde{\psi}^*(\vec{a})\tilde{\psi}(\vec{a} - \vec{x}) d^2\vec{a} \\ &= \langle \tilde{\psi}_{\vec{\Omega}} | \tilde{\psi}_{\vec{x}} \rangle, \end{aligned} \quad (15)$$

where the coordinate transformation  $\vec{a} \rightarrow \sigma\vec{a}$  is made in the second equality, the definition of  $\tilde{\psi}(\vec{x})$  is used for the third equality, and we define  $|\tilde{\psi}_{\vec{x}}\rangle = \int_{-\infty}^{\infty} \int_{-\infty}^{\infty} \tilde{\psi}(\vec{x})|\vec{x}\rangle d^2\vec{x}$  for the final equality.

Likewise, given an arbitrary orthonormalized basis with eigenvectors  $|\phi_m\rangle$ , the normalization condition  $\int_{-\infty}^{\infty} \int_{-\infty}^{\infty} \phi_m(\vec{x})^* \phi_n(\vec{x}) d^2\vec{x} = \delta_{m,n}$  results in the non-dimensionalized basis functions  $\tilde{\phi}_m(\vec{x}) = \sigma\phi_m(\sigma\vec{x})$ . Defining  $\tilde{c}_{m,n}(\vec{x}) = c_{m,n}(\sigma\vec{x})$ , analogous steps to those in Eq. (15) can be used to show that

$$\begin{aligned} \tilde{c}_{m,n}(\vec{x}) &= \int_{-\infty}^{\infty} \int_{-\infty}^{\infty} \tilde{\phi}_m^*(\vec{a})\tilde{\phi}_n(\vec{a} - \vec{x}) d^2\vec{a} \\ &\quad \times \int_{-\infty}^{\infty} \int_{-\infty}^{\infty} \tilde{\psi}^*(\vec{a} - \vec{x})\tilde{\phi}_n(\vec{a}) d^2\vec{a} \\ &= \langle \tilde{\phi}_m | \tilde{\psi}_{\vec{x}} \rangle \langle \tilde{\psi}_{\vec{x}} | \tilde{\phi}_n \rangle, \end{aligned} \quad (16)$$

where  $|\tilde{\phi}_m\rangle = \int_{-\infty}^{\infty} \int_{-\infty}^{\infty} \tilde{\phi}_m(\vec{x})|\vec{x}\rangle d^2\vec{x}$ .

### The QCE for Two Incoherent Sub-Rayleigh Objects

The PAD basis representation on an everywhere even PSF ensures that all basis functions are either even or odd in both  $x$  and  $y$ , i.e.,  $\phi_m(\vec{x}) = (-1)^{p_m} \phi_m(-\vec{x})$ , where

$p_m = k_m + l_m$  is determined by  $m$  according to Table I. Since this implies  $c_{m,n}(\vec{x}) = (-1)^{p_m+p_n} [c_{m,n}(\vec{a}-\vec{x})]_{\vec{a}=\vec{\Omega}}$ , the density matrix elements of a quantum state of form Eq. (3) can be written as

$$d_{j,m,n} = (-1)^{p_m+p_n} \left[ \frac{1}{\mu^2} m_j \left( \frac{\vec{x}}{\mu} \right) ** c_{m,n}(\vec{x}) \right]_{\vec{x}=\vec{\Omega}}, \quad (17)$$

where the operator  $**$  represents a 2D convolution. By the convolution theorem along two dimensions,

$$\frac{1}{\mu^2} m_j \left( \frac{\vec{x}}{\mu} \right) ** c_{m,n}(\vec{x}) = \mathcal{F}_{\vec{x}}^{-1} \{ M_j(\vec{X}_{\text{obj}}) C_{m,n}(\vec{X}) \}, \quad (18)$$

where  $\mathcal{F}_{\vec{x}}^{-1}$  represents an inverse 2D Fourier transform over the image-plane Fourier domain coordinates  $\vec{X} = \{X, Y\}$ , where  $\vec{X}_{\text{obj}} = \mu\vec{X}$ , and where  $M_j(\vec{X}_{\text{obj}})$  and  $C_{m,n}(\vec{X})$  denote the respective 2D characteristic functions of  $m_j(\vec{x}_{\text{obj}})$  and  $c_{m,n}(\vec{x})$ .

The characteristic function of the normalized radiant exitance profile is defined by the object-plane Fourier transform

$$\begin{aligned} M_j(\vec{X}_{\text{obj}}) &= \int_{-\infty}^{\infty} \int_{-\infty}^{\infty} m_j(\vec{x}_{\text{obj}}) e^{-i(\vec{x}_{\text{obj}} \cdot \vec{X}_{\text{obj}})} d^2\vec{x}_{\text{obj}} \\ &= \int_{-\infty}^{\infty} \int_{-\infty}^{\infty} \tilde{m}_j(\vec{x}_{\text{obj}}) e^{-i\theta(\vec{x}_{\text{obj}} \cdot \vec{X}_{\text{obj}})} d^2\vec{x}_{\text{obj}}, \end{aligned} \quad (19)$$

where the second line is found by making the coordinate transformation  $\vec{x}_{\text{obj}} \rightarrow \theta\vec{x}_{\text{obj}}$  and applying the definition of  $\tilde{m}_j(\vec{x}_{\text{obj}})$ . Taking a two-dimensional Taylor series expansion about  $\vec{X}_{\text{obj}} = \vec{\Omega}$ ,

$$\begin{aligned} M_j(\vec{X}_{\text{obj}}) &= \sum_{k,l=0}^{\infty} \frac{X_{\text{obj}}^k Y_{\text{obj}}^l}{k!l!} \left[ \frac{\partial^{k+l} M_j(\vec{X}_{\text{obj}})}{\partial X_{\text{obj}}^k \partial Y_{\text{obj}}^l} \right]_{\vec{X}_{\text{obj}}=\vec{\Omega}} \\ &= \sum_{k,l=0}^{\infty} \frac{X_{\text{obj}}^k Y_{\text{obj}}^l}{k!l!} (-i\theta)^{k+l} \\ &\quad \times \int_{-\infty}^{\infty} \int_{-\infty}^{\infty} x_{\text{obj}}^k y_{\text{obj}}^l \tilde{m}_j(\vec{x}_{\text{obj}}) d^2\vec{x}_{\text{obj}} \\ &= \sum_{k,l=0}^{\infty} \frac{X^k Y^l}{k!l!} (-i\mu\theta)^{k+l} m_{j,x_{\text{obj}}^k y_{\text{obj}}^l}. \end{aligned} \quad (20)$$

By the linearity of the Fourier transform, the inverse 2D transform in Eq. 18 can be evaluated term by term in the Taylor series from Eq. 20. Setting aside all factors with no  $\vec{X}$  dependence, the remaining inverse 2D Fourier transform in each term evaluates at the origin of the image plane to

$$\begin{aligned} \left[ \mathcal{F}_{\vec{x}}^{-1} \{ X^k Y^l C_{m,n}(\vec{X}) \} \right]_{\vec{x}=\vec{\Omega}} &= (-i)^{k+l} \left[ \frac{\partial^{k+l} c_{m,n}(\vec{x})}{\partial x^k \partial y^l} \right]_{\vec{x}=\vec{\Omega}} \\ &= \frac{(-i)^{k+l}}{\sigma^{k+l}} \left[ \frac{\partial^{k+l} \tilde{c}_{m,n}(\vec{x})}{\partial x^k \partial y^l} \right]_{\vec{x}=\vec{\Omega}}, \end{aligned} \quad (21)$$

where the second line is found by making the coordinate transformation  $\vec{x} \rightarrow \sigma \vec{x}$  and applying the definition  $\tilde{c}_{m,n}(\vec{x}) = c_{m,n}(\sigma \vec{x})$ . These steps taken together result in Eq. 8 in the main text.

Since we seek a lowest order result in the regime where  $\gamma \ll 1$ , we will focus on the terms in  $d_{j,m,n}$  up to  $O(\gamma^2)$ , recalling the assumption that the first moments in  $x$  and  $y$  of the normalized radiant exitance distributions are zero (i.e.,  $m_{j,x_{\text{obj}}} = 0$  and  $m_{j,y_{\text{obj}}} = 0$ , and therefore  $m_{j,x_{\text{obj}}y_{\text{obj}}} = 0$ ). In the PAD basis, where  $|\phi_0\rangle = |\psi_{\vec{x}}\rangle$ , we have  $c_{0,0}(\vec{x}) = |\Gamma(\vec{x})|^2$  and  $[c_{m,n}(\vec{x})]_{\vec{x}=\vec{\Omega}} = \delta_{m,0}\delta_{n,0}$ . We therefore find that a state  $\rho_j$  can be expanded in powers of  $\gamma$  as

$$\begin{aligned} \rho_j = & |\phi_0\rangle\langle\phi_0| + \frac{\gamma^2}{2} \sum_{m,n=0}^{\infty} |\phi_m\rangle\langle\phi_n| (-1)^{p_m+p_n} \\ & \times \left( m_{j,x_{\text{obj}}}^2 \left[ \frac{\partial^2 \tilde{c}_{m,n}(\vec{x})}{\partial x^2} \right]_{\vec{x}=\vec{\Omega}} \right. \\ & \left. + m_{j,y_{\text{obj}}}^2 \left[ \frac{\partial^2 \tilde{c}_{m,n}(\vec{x})}{\partial y^2} \right]_{\vec{x}=\vec{\Omega}} \right) + O(\gamma^3). \end{aligned} \quad (22)$$

To analyze the states  $\rho_1$  and  $\rho_2$ , we must evaluate the second-order derivatives in Eq. 22, which can be ex-

panded using Eq. (16) to find

$$\begin{aligned} \left[ \frac{\partial^2 \tilde{c}_{m,n}(\vec{x})}{\partial x^2} \right]_{\vec{x}=\vec{\Omega}} &= \left[ \frac{\partial^2}{\partial x^2} \left( \langle \tilde{\phi}_m | \tilde{\psi}_{\vec{x}} \rangle \langle \tilde{\psi}_{\vec{x}} | \tilde{\phi}_n \rangle \right) \right]_{\vec{x}=\vec{\Omega}} \\ &= \langle \tilde{\phi}_m | \partial_{x^{(2)}} \tilde{\psi}_{\vec{\Omega}} \rangle \langle \tilde{\psi}_{\vec{\Omega}} | \tilde{\phi}_n \rangle \\ &\quad + 2 \langle \tilde{\phi}_m | \partial_{x^{(1)}} \tilde{\psi}_{\vec{\Omega}} \rangle \langle \partial_{x^{(1)}} \tilde{\psi}_{\vec{\Omega}} | \tilde{\phi}_n \rangle \\ &\quad + \langle \tilde{\phi}_m | \tilde{\psi}_{\vec{\Omega}} \rangle \langle \partial_{x^{(2)}} \tilde{\psi}_{\vec{\Omega}} | \tilde{\phi}_n \rangle \end{aligned} \quad (23)$$

and the analogous quantity involving derivatives with respect to  $y$ .

The inner products in Eq. 23 can be evaluated by performing the Gram-Schmidt orthogonalization procedure to relate the PAD basis functions to the PSF. The Gram-Schmidt process is equivalent to a QR decomposition  $\Psi = \Phi W$  in the single-photon Hilbert space  $\mathcal{H}$ , where the ‘‘PSF derivative’’ vectors

$$|\partial_{x^{k_m} y^{l_m}} \tilde{\psi}_{\vec{\Omega}}\rangle = \left[ \int_{-\infty}^{\infty} \int_{-\infty}^{\infty} \frac{\partial^{k_m+l_m}}{\partial x^{k_m} \partial y^{l_m}} \tilde{\psi}(\vec{a}-\vec{x}) |\vec{a}\rangle d^2 \vec{a} \right]_{\vec{x}=\vec{\Omega}} \quad (24)$$

define the columns of  $\Psi$ ,  $\Phi$  is a unitary matrix with the PAD basis vectors  $|\tilde{\phi}_m\rangle$  as its columns, and  $W$  is a non-singular upper diagonal matrix. In the PAD basis representation,  $\Phi$  is an infinite-dimensional identity matrix, so the columns of  $\Psi = W$  give the PSF derivative vectors in terms of the PAD basis vectors. This decomposition leads to a natural indexing of the PAD basis elements (Table I) according to ascending total number of derivatives  $p_m$  taken in the vectors  $|\partial_{x^{k_m} y^{l_m}} \tilde{\psi}_{\vec{\Omega}}\rangle$ .

Performing the Gram-Schmidt procedure defines the PAD basis vectors

$$|\tilde{\phi}_m\rangle = \sum_{n=0}^m w_{n,m} |\partial_{x^{k_n} y^{l_n}} \tilde{\psi}_{\vec{\Omega}}\rangle, \quad (25)$$

where

$$\begin{aligned}
w_{0,0} &= 1 \\
w_{1,1} &= \frac{1}{\sqrt{\langle \partial_x \tilde{\psi}_{\bar{\Omega}} | \partial_x \tilde{\psi}_{\bar{\Omega}} \rangle}} \\
w_{2,2} &= \frac{1}{\sqrt{\langle \partial_y \tilde{\psi}_{\bar{\Omega}} | \partial_y \tilde{\psi}_{\bar{\Omega}} \rangle}} \\
w_{0,3} &= - \frac{\langle \tilde{\psi}_{\bar{\Omega}} | \partial_{x^2} \tilde{\psi}_{\bar{\Omega}} \rangle}{\sqrt{\langle \partial_{x^2} \tilde{\psi}_{\bar{\Omega}} | \partial_{x^2} \tilde{\psi}_{\bar{\Omega}} \rangle - |\langle \tilde{\psi}_{\bar{\Omega}} | \partial_{x^2} \tilde{\psi}_{\bar{\Omega}} \rangle|^2}} \\
w_{3,3} &= \frac{1}{\sqrt{\langle \partial_{x^2} \tilde{\psi}_{\bar{\Omega}} | \partial_{x^2} \tilde{\psi}_{\bar{\Omega}} \rangle - |\langle \tilde{\psi}_{\bar{\Omega}} | \partial_{x^2} \tilde{\psi}_{\bar{\Omega}} \rangle|^2}} \\
w_{4,4} &= \frac{1}{\sqrt{\langle \partial_{xy} \tilde{\psi}_{\bar{\Omega}} | \partial_{xy} \tilde{\psi}_{\bar{\Omega}} \rangle}} \\
w_{0,5} &= - \frac{\langle \tilde{\psi}_{\bar{\Omega}} | \partial_{y^2} \tilde{\psi}_{\bar{\Omega}} \rangle - \langle \tilde{\psi}_{\bar{\Omega}} | \partial_{x^2} \tilde{\psi}_{\bar{\Omega}} \rangle \langle \tilde{\phi}_3 | \partial_{y^2} \tilde{\psi}_{\bar{\Omega}} \rangle}{\sqrt{\langle \partial_{y^2} \tilde{\psi}_{\bar{\Omega}} | \partial_{y^2} \tilde{\psi}_{\bar{\Omega}} \rangle - |\langle \tilde{\psi}_{\bar{\Omega}} | \partial_{y^2} \tilde{\psi}_{\bar{\Omega}} \rangle|^2 - |\langle \tilde{\phi}_3 | \partial_{y^2} \tilde{\psi}_{\bar{\Omega}} \rangle|^2}} \\
w_{3,5} &= - \frac{\langle \tilde{\phi}_3 | \partial_{y^2} \tilde{\psi}_{\bar{\Omega}} \rangle}{\sqrt{\langle \partial_{y^2} \tilde{\psi}_{\bar{\Omega}} | \partial_{y^2} \tilde{\psi}_{\bar{\Omega}} \rangle - |\langle \tilde{\psi}_{\bar{\Omega}} | \partial_{y^2} \tilde{\psi}_{\bar{\Omega}} \rangle|^2 - |\langle \tilde{\phi}_3 | \partial_{y^2} \tilde{\psi}_{\bar{\Omega}} \rangle|^2}} \\
w_{5,5} &= - \frac{1}{\sqrt{\langle \partial_{y^2} \tilde{\psi}_{\bar{\Omega}} | \partial_{y^2} \tilde{\psi}_{\bar{\Omega}} \rangle - |\langle \tilde{\psi}_{\bar{\Omega}} | \partial_{y^2} \tilde{\psi}_{\bar{\Omega}} \rangle|^2 - |\langle \tilde{\phi}_3 | \partial_{y^2} \tilde{\psi}_{\bar{\Omega}} \rangle|^2}}
\end{aligned} \tag{26}$$

give the matrix elements of  $W^{-1}$  in the PAD basis. In matrix form,

$$W^{-1} = \begin{pmatrix} w_{0,0} & 0 & 0 & w_{0,3} & 0 & w_{0,5} & \cdots \\ 0 & w_{1,1} & 0 & 0 & 0 & 0 & \cdots \\ 0 & 0 & w_{2,2} & 0 & 0 & 0 & \cdots \\ 0 & 0 & 0 & w_{3,3} & 0 & w_{3,5} & \cdots \\ 0 & 0 & 0 & 0 & w_{4,4} & 0 & \cdots \\ 0 & 0 & 0 & 0 & 0 & w_{5,5} & \cdots \\ \vdots & \vdots & \vdots & \vdots & \vdots & \vdots & \ddots \end{pmatrix}, \tag{27}$$

where we show just the subspace  $\mathcal{H}_6$  corresponding to the first six PAD basis vectors according to Table I. All other coefficients  $w_{m,n}$  for  $0 \leq m \leq 5$  and  $0 \leq n \leq 5$  are zero due to mismatched even-odd parity between the integer pairs  $(k_m, k_n)$  and/or  $(l_m, k_n)$  in Eq. 25. Since the Schur

complement of any block of an upper triangular matrix is simply given by that matrix block, the inverse of any diagonal block of an upper triangular matrix is equal to the same diagonal block of the inverse of the matrix. Inverting  $W^{-1}$ , we find that the matrix

$$W = \begin{pmatrix} W_{0,0} & 0 & 0 & W_{0,3} & 0 & W_{0,5} & \cdots \\ 0 & W_{1,1} & 0 & 0 & 0 & 0 & \cdots \\ 0 & 0 & W_{2,2} & 0 & 0 & 0 & \cdots \\ 0 & 0 & 0 & W_{3,3} & 0 & W_{3,5} & \cdots \\ 0 & 0 & 0 & 0 & W_{4,4} & 0 & \cdots \\ 0 & 0 & 0 & 0 & 0 & W_{5,5} & \cdots \\ \vdots & \vdots & \vdots & \vdots & \vdots & \vdots & \ddots \end{pmatrix} \tag{28}$$

with

$$\begin{aligned}
W_{0,0} &= \frac{1}{w_{0,0}} = 1 \\
W_{1,1} &= \frac{1}{w_{1,1}} = \sqrt{\langle \partial_x \tilde{\psi}_{\bar{\Omega}} | \partial_x \tilde{\psi}_{\bar{\Omega}} \rangle} \\
W_{2,2} &= \frac{1}{w_{2,2}} = \sqrt{\langle \partial_y \tilde{\psi}_{\bar{\Omega}} | \partial_y \tilde{\psi}_{\bar{\Omega}} \rangle} \\
W_{0,3} &= -\frac{w_{0,3}}{w_{0,0}w_{3,3}} = \langle \tilde{\psi}_{\bar{\Omega}} | \partial_{x^2} \tilde{\psi}_{\bar{\Omega}} \rangle \\
W_{3,3} &= \frac{1}{w_{3,3}} = \sqrt{\langle \partial_{x^2} \tilde{\psi}_{\bar{\Omega}} | \partial_{x^2} \tilde{\psi}_{\bar{\Omega}} \rangle - |\langle \tilde{\psi}_{\bar{\Omega}} | \partial_{x^2} \tilde{\psi}_{\bar{\Omega}} \rangle|^2} \\
W_{4,4} &= \frac{1}{w_{4,4}} = \sqrt{\langle \partial_{xy} \tilde{\psi}_{\bar{\Omega}} | \partial_{xy} \tilde{\psi}_{\bar{\Omega}} \rangle} \\
W_{0,5} &= \frac{w_{0,3}w_{3,5} - w_{0,5}w_{3,3}}{w_{0,0}w_{3,3}w_{5,5}} = \langle \tilde{\psi}_{\bar{\Omega}} | \partial_{y^2} \tilde{\psi}_{\bar{\Omega}} \rangle \\
W_{3,5} &= -\frac{w_{3,5}}{w_{3,3}w_{5,5}} = \langle \partial_{x^2} \tilde{\psi}_{\bar{\Omega}} | \partial_{y^2} \tilde{\psi}_{\bar{\Omega}} \rangle - \langle \partial_{x^2} \tilde{\psi}_{\bar{\Omega}} | \tilde{\psi}_{\bar{\Omega}} \rangle \langle \tilde{\psi}_{\bar{\Omega}} | \partial_{y^2} \tilde{\psi}_{\bar{\Omega}} \rangle \\
W_{5,5} &= \frac{1}{w_{5,5}} = \sqrt{\langle \partial_{y^2} \tilde{\psi}_{\bar{\Omega}} | \partial_{y^2} \tilde{\psi}_{\bar{\Omega}} \rangle - |\langle \tilde{\psi}_{\bar{\Omega}} | \partial_{y^2} \tilde{\psi}_{\bar{\Omega}} \rangle|^2 - |\langle \tilde{\phi}_3 | \partial_{y^2} \tilde{\psi}_{\bar{\Omega}} \rangle|^2}
\end{aligned} \tag{29}$$

represents on its columns the non-orthonormal PSF derivative vectors in the orthonormal PAD basis, as in

$$|\partial_{x^k y^l m} \tilde{\psi}_{\bar{\Omega}}\rangle = \sum_{n=0}^m W_{n,m} |\tilde{\phi}_n\rangle. \tag{30}$$

These steps show that the  $m^{\text{th}}$  PSF derivative vector depends on only the basis vectors  $|\tilde{\phi}_n\rangle$  for which  $n \leq m$ .

Using Eq. (30) and  $\langle \tilde{\phi}_m | \tilde{\phi}_n \rangle = \delta_{m,n}$ , we rewrite the density matrix elements [Eq. (8)] in the PAD basis as

$$\begin{aligned}
d_{j,0,0} &= 1 + \text{Re}(m_{j,x_{\text{obj}}^2} W_{0,3} + m_{j,y_{\text{obj}}^2} W_{0,5}) \gamma^2 + O(\gamma^3) \\
&= 1 - (m_{j,x_{\text{obj}}^2} \Gamma_{x^2} + m_{j,y_{\text{obj}}^2} \Gamma_{y^2}) \gamma^2 + O(\gamma^3) \\
d_{j,1,1} &= m_{j,x_{\text{obj}}^2} W_{1,1} \gamma^2 + O(\gamma^3) \\
&= m_{j,x_{\text{obj}}^2} \Gamma_{x^2} \gamma^2 + O(\gamma^3) \\
d_{j,2,2} &= m_{j,y_{\text{obj}}^2} W_{2,2} \gamma^2 + O(\gamma^3) \\
&= m_{j,y_{\text{obj}}^2} \Gamma_{y^2} \gamma^2 + O(\gamma^3) \\
d_{j,3,0} &= \frac{1}{2} (m_{j,x_{\text{obj}}^2} W_{3,3} + m_{j,y_{\text{obj}}^2} W_{3,5}) \gamma^2 + O(\gamma^3) \\
d_{j,0,3} &= \frac{1}{2} (m_{j,x_{\text{obj}}^2} w_{3,3}^* + m_{j,y_{\text{obj}}^2} w_{3,5}^*) \gamma^2 + O(\gamma^3) \\
d_{j,5,0} &= \frac{1}{2} m_{j,y_{\text{obj}}^2} W_{5,5} \gamma^2 + O(\gamma^3) \\
d_{j,0,5} &= \frac{1}{2} m_{j,y_{\text{obj}}^2} w_{5,5}^* \gamma^2 + O(\gamma^3),
\end{aligned} \tag{31}$$

where all other matrix elements are  $O(\gamma^3)$ . The relationships  $\text{Re}(W_{0,3}) = -\Gamma_{x^2}$  and  $\text{Re}(W_{0,5}) = -\Gamma_{y^2}$  are given as an identity in Ref. [25], while  $W_{1,1}^2 = \Gamma_{x^2}$  (and likewise  $W_{2,2}^2 = \Gamma_{y^2}$ ) can be derived by taking 2nd derivatives on

either side of the PSF normalization condition and exchanging the order of integration and differentiation:

$$\begin{aligned}
0 &= \int_{-\infty}^{\infty} \int_{-\infty}^{\infty} \frac{\partial^2}{\partial x^2} |\tilde{\psi}(\vec{x})|^2 d^2 \vec{x} \\
&= \int_{-\infty}^{\infty} \int_{-\infty}^{\infty} 2 \left| \frac{\partial \tilde{\psi}(\vec{x})}{\partial x} \right|^2 + 2 \text{Re} \left( \tilde{\psi}^*(\vec{x}) \frac{\partial^2 \tilde{\psi}(\vec{x})}{\partial x^2} \right) d^2 \vec{x} \\
&= 2(W_{1,1}^2 - \Gamma_{x^2}).
\end{aligned} \tag{32}$$

Note that if the PSF is separable in  $x$  and  $y$  i.e.,  $\psi(\vec{x}) = \Xi(x)\Upsilon(y)$ , then  $W_{3,5} = 0$ .

With the states  $\rho_1$  and  $\rho_2$  [Eq. (3)] represented in the finite dimensional PAD basis defined on the truncated subspace  $\mathcal{H}_6$ , we can directly evaluate the quantum Chernoff exponent [Eq. (6)] to lowest non-vanishing order in  $\gamma$  using our accompanying work on perturbation theory for common entropic and distance measures in quantum information theory [28]. We first decompose both density matrices into  $\rho_j = \rho_0 + \nu_j$ , where  $\rho_0 = |\phi_0\rangle\langle\phi_0|$  is a pure state and  $\nu_1$  and  $\nu_2$  are zero-trace perturbation matrices with spectral norms  $\|\nu_j\| = O(\gamma^2)$ . We additionally block decompose the truncated Hilbert space as  $\mathcal{H}_6 = \mathcal{H}_1 \oplus \mathcal{H}_5$ , where  $\mathcal{H}_1$  is the 1-dimensional subspace of  $\mathcal{H}_6$  corresponding to the support of the pure state  $\rho_0$  and  $\mathcal{H}_5$  is the kernel of  $\rho_0$  on  $\mathcal{H}_6$ . We denote the resulting matrix decompositions as

$$\begin{aligned}
\rho_0 &= \begin{pmatrix} 1 & 0 \\ 0 & 0 \end{pmatrix} \\
\nu_j &= \begin{pmatrix} \nu_{j,B} & \nu_{j,C} \\ \nu_{j,C}^\dagger & \nu_{j,D} \end{pmatrix}.
\end{aligned} \tag{33}$$

Following the perturbation theory for perturbations that extend the support of the original states [28], the QCE

$$\begin{aligned} \xi_s(\rho_1, \rho_2) = & - \min_{s \in [0,1]} s \text{Tr}[\nu_{1,B}] + (1-s) \text{Tr}[\nu_{2,B}] \\ & + \text{Tr}[\nu_{1,D}^s \nu_{2,D}^{1-s}] + O(\max(\|\nu_1\|, \|\nu_2\|)^2) \end{aligned} \quad (34)$$

can be evaluated by reading off the matrix elements of  $\nu_{1,B}$ ,  $\nu_{2,B}$ ,  $\nu_{1,D}$  and  $\nu_{2,D}$  using Eq. 31. The result is Eq. 10 in the main text.

### Direct Imaging

For a continuously valued measurement, the classical Chernoff exponent takes the form

$$\xi_{\text{C,Direct}} = -\log \left[ \min_{0 \leq s \leq 1} Q_s \right] \quad (35)$$

with

$$\begin{aligned} Q_s &= \int_{-\infty}^{\infty} \int_{-\infty}^{\infty} P(\vec{x}|\rho_1)^s P(\vec{x}|\rho_2)^{1-s} d^2 \vec{x} \\ &= \int_{-\infty}^{\infty} \int_{-\infty}^{\infty} (\sigma^2 P(\sigma \vec{x}|\rho_1))^s (\sigma^2 P(\sigma \vec{x}|\rho_2))^{1-s} d^2 \vec{x}, \end{aligned} \quad (36)$$

where in the second line we have made the coordinate transformation  $\vec{x} \rightarrow \sigma \vec{x}$  and distributed the factor  $\sigma^2$ .

From Eq. (2), we have

$$\begin{aligned} P(\vec{x}|\rho_j) &= \text{Tr}[\rho_j |\vec{x}\rangle \langle \vec{x}| d^2 \vec{x}] \\ &= \int_{-\infty}^{\infty} \int_{-\infty}^{\infty} \frac{1}{\mu^2} m_j \left( \frac{\vec{a}}{\mu} \right) \langle \vec{x} | \psi_{\vec{a}} \rangle \langle \psi_{\vec{a}} | \vec{x} \rangle d^2 \vec{a} \\ &= \frac{1}{\mu^2} m_j \left( \frac{\vec{x}}{\mu} \right) * |\psi(\vec{x})|^2, \end{aligned} \quad (37)$$

which is consistent with the standard result from classical image science that the image plane intensity distribution in an incoherent imaging context is given by a 2D convolution of the object radiant exitance and the incoherent PSF [2]. By the convolution theorem,  $(1/\mu^2) m_j(\vec{x}/\mu) ** |\psi(\vec{x})|^2 = \mathcal{F}_{\vec{x}}^{-1} \{ M_j(\vec{X}_{\text{obj}}) \Psi(\vec{X}) \}$ , where  $\Psi(\vec{X})$  is the 2D characteristic function of the incoherent PSF  $|\psi(\vec{x})|^2$ . Using Eq. (20) and evaluating the inverse 2D Fourier transform via similar methods to those used for Eq. (21), we find that the relevant probability density functions for the integrand of Eq. (36) have the form

$$P(\sigma \vec{x}|\rho_j) = \frac{1}{\sigma^2} \sum_{k,l=0}^{\infty} (-1)^{k+l} \frac{\gamma^{k+l}}{k!l!} m_{j,x_{\text{obj}}^k y_{\text{obj}}^l} \psi_{x^k y^l}(\vec{x}) \quad (38)$$

where

$$\psi_{x^k y^l}(\vec{x}) = \frac{\partial^{k+l} |\tilde{\psi}(\vec{x})|^2}{\partial x^k \partial y^l}. \quad (39)$$

In order to calculate the Chernoff exponent in the limit  $\gamma \ll 1$ , we generalize the methods from Ref. [9] and expand the integrand of  $Q_s$  using the Taylor series

$$\begin{aligned} f(\gamma)^s g(\gamma)^{1-s} &= f_0 + (s f_2 + (1-s) g_2) \gamma^2 \\ &\quad + (s f_3 + (1-s) g_3) \gamma^3 \\ &\quad + \left[ s f_4 + (1-s) g_4 \right. \\ &\quad \left. - \frac{1}{2 f_0} s(1-s)(f_2 - g_2)^2 \right] \gamma^4 + O(\gamma^5) \end{aligned} \quad (40)$$

where  $f(\gamma) \equiv \sum_{n=0}^{\infty} f_n \gamma^n = \sigma^2 P(\sigma \vec{x}|\rho_0)$  and  $g(\gamma) \equiv \sum_{n=0}^{\infty} g_n \gamma^n = \sigma^2 P(\sigma \vec{x}|\rho_1)$ , and where we used  $g_0 = f_0$  and  $g_1 = f_1 = 0$  since  $m_{j,x_{\text{obj}}} = m_{j,y_{\text{obj}}} = m_{j,x_{\text{obj}} y_{\text{obj}}} = 0$ . First, we consider only terms in  $Q_s$  up to third order in  $\gamma$ . Using Eq. (38) to determine the coefficients  $f_n$  and  $g_n$ , Eqs. (36) and (40) result in

$$\begin{aligned} Q_s &= \int_{-\infty}^{\infty} \int_{-\infty}^{\infty} |\tilde{\psi}(\vec{x})|^2 \\ &\quad + \frac{1}{2} [(s m_{1,x_{\text{obj}}^2} + (1-s) m_{2,x_{\text{obj}}^2}) \psi_{x^2}(\vec{x}) \\ &\quad + (s m_{1,y_{\text{obj}}^2} + (1-s) m_{2,y_{\text{obj}}^2}) \psi_{y^2}(\vec{x})] \gamma^2 \\ &\quad + \frac{1}{6} [(s m_{1,x_{\text{obj}}^3} + (1-s) m_{2,x_{\text{obj}}^3}) \psi_{x^3}(\vec{x}) \\ &\quad + (s m_{1,y_{\text{obj}}^3} + (1-s) m_{2,y_{\text{obj}}^3}) \psi_{y^3}(\vec{x})] \gamma^3 d^2 \vec{x} + O(\gamma^4). \end{aligned} \quad (41)$$

After distributing the integral to each of the terms, we note that

$$\int_{-\infty}^{\infty} \int_{-\infty}^{\infty} \psi_{x^k y^l}(\vec{x}) d^2 \vec{x} = \delta_{k,0} \delta_{l,0}, \quad (42)$$

which can be shown by exchanging the order of integration and differentiation and using the normalization condition on  $\tilde{\psi}(\vec{x})$  [9]. Thus,  $Q_s = 1$  for all values of  $s$ , and  $\xi_{\text{C,Direct}} = O(\gamma^4)$ , while the quantum Chernoff exponent has nonzero  $\gamma^2$  terms in the sub-Rayleigh limit [Eq. (10)]. This implies at least a quadratic scaling difference between the achievable error exponent when using direct imaging compared with the quantum limit for any sub-diffraction binary object discrimination task with an arbitrary 2D aperture.

To get a closed form expression for the direct detection classical Chernoff exponent to lowest non-zero order in  $\gamma \ll 1$  for a restricted class of PSFs (see below), we expand  $Q_s$  to fourth order in  $\gamma$  using all of the terms given in Eq. (40). After integrating the  $\gamma^2$  and  $\gamma^3$  terms

of  $Q_s$  to zero as before, we have

$$\begin{aligned}
Q_s = & \int_{-\infty}^{\infty} \int_{-\infty}^{\infty} \left| \tilde{\psi}(\vec{x}) \right|^2 \\
& + \frac{1}{24} \left[ (sm_{1,x_{\text{obj}}}^4 + (1-s)m_{2,x_{\text{obj}}}^4) \psi_{x^4}(\vec{x}) \right. \\
& + 6(sm_{1,x_{\text{obj}}^2 y_{\text{obj}}^2} + (1-s)m_{2,x_{\text{obj}}^2 y_{\text{obj}}^2}) \psi_{x^2 y^2}(\vec{x}) \\
& + (sm_{1,y_{\text{obj}}}^4 + (1-s)m_{2,y_{\text{obj}}}^4) \psi_{y^4}(\vec{x}) \\
& - \frac{3s(1-s)}{\left| \tilde{\psi}(\vec{x}) \right|^2} \left( (m_{1,x_{\text{obj}}^2} - m_{2,x_{\text{obj}}^2}) \psi_{x^2}(\vec{x}) \right. \\
& \left. \left. + (m_{1,y_{\text{obj}}^2} - m_{2,y_{\text{obj}}^2}) \psi_{y^2}(\vec{x}) \right)^2 \right] \gamma^4 d^2 \vec{x} + O(\gamma^5).
\end{aligned} \tag{43}$$

Applying Eq. 42, we find

$$Q_s = 1 - \frac{s(1-s)\mathcal{K}}{8} \gamma^4 + O(\gamma^5), \tag{44}$$

where  $\mathcal{K}$  is given by Eq. 13 in the main text. Minimizing  $Q_s$  is then equivalent to maximizing  $s(1-s)$ , so  $s = 1/2$  and the Chernoff exponent is given by Eq. 12. As an aside, if the PSF is separable in  $x$  and  $y$ , i.e.,  $\psi(\vec{x}) = \Xi(x)\Upsilon(y)$ , the integral  $\int_{-\infty}^{\infty} \int_{-\infty}^{\infty} \left| \tilde{\psi}(\vec{x}) \right|^{-2} \psi_{x^2}(\vec{x}) \psi_{y^2}(\vec{x}) d^2 \vec{x} = 0$  follows from  $\psi_{x^2}(\vec{x}) \psi_{y^2}(\vec{x}) = \psi_{x^2 y^2}(\vec{x})$  and Eq. 42, and therefore

$$\xi_{\text{C,Direct}} = \frac{\mathcal{K}_x + \mathcal{K}_y}{32} \gamma^4 + O(\gamma^5). \tag{45}$$

where

$$\begin{aligned}
\mathcal{K}_x = & (m_{1,x_{\text{obj}}^2} - m_{2,x_{\text{obj}}^2})^2 \int_{-\infty}^{\infty} \int_{-\infty}^{\infty} \frac{\psi_{x^2}(\vec{x})^2}{\left| \tilde{\psi}(\vec{x}) \right|^2} d^2 \vec{x} \\
\mathcal{K}_y = & (m_{1,y_{\text{obj}}^2} - m_{2,y_{\text{obj}}^2})^2 \int_{-\infty}^{\infty} \int_{-\infty}^{\infty} \frac{\psi_{y^2}(\vec{x})^2}{\left| \tilde{\psi}(\vec{x}) \right|^2} d^2 \vec{x}.
\end{aligned} \tag{46}$$

It is very important to note that this closed form expression for the direct imaging Chernoff exponent to lowest nonzero order in  $\gamma$  [Eq. (12)] does not hold for all PSFs. Namely, the presence of the factor  $|\tilde{\psi}(\vec{x})|^{-2}$  in  $\mathcal{K}$  results in a diverging integral if the coherent PSF  $\psi(\vec{x})$  is exactly zero at any point  $\vec{x} \in \mathbb{R}^2$ . Most significantly, this includes the Airy disk PSF associated with a hard circular aperture [2], a ubiquitous aperture geometry for realistic imaging systems. A similar situation was encountered in Ref. [33], which pointed out that the sub-Rayleigh scaling of the Fisher information for estimating an object parameter cannot be evaluated by expanding the integrand as a Taylor series and integrating individual terms when there are zeros in the PSF. Likewise, our integration of the individual terms of Eq. (43) is invalid for such PSFs. However, our result differs in kind from that of Ref. [33], which reported a factor of  $\gamma$  (in our notation)

improvement in the scaling of the direct imaging Fisher information using a hard aperture compared with that using a Gaussian attenuated aperture model. In the case of binary hypothesis testing, we find that the integrals of the individual terms of  $Q_s$  up to third order in  $\gamma$  always converge [Eq. (41)], so the result  $\xi_{\text{C,Direct}} = O(\gamma^4)$  holds for any PSF. Therefore, while we cannot write down a closed form expression for  $\xi_{\text{C,Direct}}$  when using an aperture with zeros in its PSF, the scaling gap between the classical and quantum Chernoff exponents is always at least quadratic in the sub-Rayleigh limit, and PSFs with zeros give no fundamental advantage for discrimination with direct imaging.

### Quantum-Optimal Measurements

We first consider a binary projective measurement with POVM elements  $\Pi_0 = |\psi_{\vec{\Omega}}\rangle\langle\psi_{\vec{\Omega}}|$  and  $\Pi_1 = \mathcal{I} - |\psi_{\vec{\Omega}}\rangle\langle\psi_{\vec{\Omega}}|$ , which can be implemented by a 2D BSPADE device [21]. From Eq. (31),

$$\begin{aligned}
P(0|\rho_j) = & d_{j,0,0} \\
= & 1 - (m_{j,x_{\text{obj}}^2} \Gamma_{x^2} + m_{j,y_{\text{obj}}^2} \Gamma_{y^2}) \gamma^2 + O(\gamma^3) \\
P(1|\rho_j) = & 1 - d_{j,0,0} \\
= & (m_{j,x_{\text{obj}}^2} \Gamma_{x^2} + m_{j,y_{\text{obj}}^2} \Gamma_{y^2}) \gamma^2 + O(\gamma^3).
\end{aligned} \tag{47}$$

We apply Eq. (5) from the main text and utilize the first order expansion  $(1+u)^v = 1 + vu + O(u^2)$  to simplify the terms  $P(0|\rho_1)^s$  and  $P(0|\rho_2)^{1-s}$ . Expanding the logarithm in Eq. (5) using  $\ln(1+u) = u + O(u^2)$ , the classical Chernoff exponent for the 2D BSPADE measurement is given by

$$\begin{aligned}
\xi_{\text{C,BSPADE}} = & \max_{0 \leq s \leq 1} \left[ s(m_{1,x_{\text{obj}}^2} \Gamma_{x^2} + m_{1,y_{\text{obj}}^2} \Gamma_{y^2}) \right. \\
& + (1-s)(m_{2,x_{\text{obj}}^2} \Gamma_{x^2} + m_{2,y_{\text{obj}}^2} \Gamma_{y^2}) \\
& - (m_{1,x_{\text{obj}}^2} \Gamma_{x^2} + m_{1,y_{\text{obj}}^2} \Gamma_{y^2})^s \\
& \left. \times (m_{2,x_{\text{obj}}^2} \Gamma_{x^2} + m_{2,y_{\text{obj}}^2} \Gamma_{y^2})^{1-s} \right] \gamma^2 \\
& + O(\gamma^3).
\end{aligned} \tag{48}$$

Unlike hypothesis tests between a point source and an arbitrary object, the 2D BSPADE measurement does not in general achieve the quantum limit [Eq. (10)] in the sub-Rayleigh limit for a binary hypothesis test between any two arbitrary objects. A few steps of algebra show that  $\xi_{\text{C,BSPADE}} = \xi_{\text{Q}}$  when the two objects have the same ellipticity, i.e., when  $m_{1,x_{\text{obj}}^2}/m_{1,y_{\text{obj}}^2} = m_{2,x_{\text{obj}}^2}/m_{2,y_{\text{obj}}^2}$ , but when this condition is not met the 2D BSPADE measurement is not quantum-optimal.

Alternatively, the POVM elements  $\Pi_0 = |\phi_0\rangle\langle\phi_0|$ ,  $\Pi_1 = |\phi_1\rangle\langle\phi_1|$ ,  $\Pi_2 = |\phi_2\rangle\langle\phi_2|$ , and  $\Pi_3 = \mathcal{I} - \Pi_0 - \Pi_1 - \Pi_2$  form a projective measurement and are constructed from

the first three eigenvectors of the PAD basis and the remaining subspace on  $\mathcal{H}$ . From Eq. (31), the measurement outcome probabilities are

$$\begin{aligned}
P(0|\rho_j) &= d_{j,0,0} \\
&= 1 - (m_{j,x_{\text{obj}}^2} \Gamma_{x^2} + m_{j,y_{\text{obj}}^2} \Gamma_{y^2}) \gamma^2 + O(\gamma^3) \\
P(1|\rho_j) &= d_{j,1,1} = m_{j,x^2} \Gamma_{x_{\text{obj}}^2} \gamma^2 + O(\gamma^3) \\
P(2|\rho_j) &= d_{j,2,2} = m_{j,y_{\text{obj}}^2} \Gamma_{y^2} \gamma^2 + O(\gamma^3) \\
P(3|\rho_j) &= 1 - d_{j,0,0} - d_{j,1,1} - d_{j,2,2} = O(\gamma^3).
\end{aligned} \tag{49}$$

Since  $\Pi_3$  has negligible outcome probability in the limit  $\gamma \ll 1$ , the fourth POVM element can be ignored in a practical implementation designed for sub-Rayleigh imaging. Using Eq. (5) from the main text and the same expansions as before, the CE of the resulting TriSPADE measurement formed by the projectors  $\Pi_0$ ,  $\Pi_1$ , and  $\Pi_2$ ,

$$\begin{aligned}
\xi_{\text{C, TriSPADE}} &= \max_{0 \leq s \leq 1} \left[ s(m_{1,x_{\text{obj}}^2} \Gamma_{x^2} + m_{1,y_{\text{obj}}^2} \Gamma_{y^2}) \right. \\
&\quad + (1-s)(m_{2,x_{\text{obj}}^2} \Gamma_{x^2} + m_{2,y_{\text{obj}}^2} \Gamma_{y^2}) \\
&\quad - m_{1,x_{\text{obj}}^2}^s m_{2,x_{\text{obj}}^2}^{1-s} \Gamma_{x^2} \\
&\quad \left. - m_{1,y_{\text{obj}}^2}^s m_{2,y_{\text{obj}}^2}^{1-s} \Gamma_{y^2} \right] \gamma^2 + O(\gamma^3),
\end{aligned} \tag{50}$$

is exactly equal to the QCE [Eq. (10) in the main text].

### Special Cases

Our results must be modified in the special case of two candidate objects that have exactly the same second moment in  $x_{\text{obj}}$  and  $y_{\text{obj}}$ . In this case, the quantities given in Eqs. (10), (12), (48), (50), and are all zero to the orders in  $\gamma$  specified, and higher order terms are needed to find relationships between these Chernoff exponents. Let  $\kappa$  be the lowest-order moment that differs between  $m_1(\vec{x}_{\text{obj}})$  and  $m_2(\vec{x}_{\text{obj}})$  in either  $x_{\text{obj}}$  or  $y_{\text{obj}}$ . For the quantum Chernoff exponent, we can start from the quantum state representation given by Eqs. (3) and (8) and keep terms up to order  $\kappa$  in  $\gamma$ , leading to the expansion

$$\begin{aligned}
\rho_j &= |\phi_0\rangle\langle\phi_0| + \frac{\gamma^\kappa}{\kappa!} \sum_{m,n=0}^{\infty} |\phi_m\rangle\langle\phi_n| (-1)^{p_m+p_n+\kappa} \\
&\quad \times \left( m_{j,x_{\text{obj}}^\kappa} \left[ \frac{\partial^\kappa \tilde{c}_{m,n}(\vec{x})}{\partial x^\kappa} \right]_{\vec{x}=\vec{\Omega}} \right. \\
&\quad \left. + m_{j,y_{\text{obj}}^\kappa} \left[ \frac{\partial^\kappa \tilde{c}_{m,n}(\vec{x})}{\partial y^\kappa} \right]_{\vec{x}=\vec{\Omega}} \right) + O(\gamma^{\kappa+1}).
\end{aligned} \tag{51}$$

Generalizing Eq. (23), the derivatives become

$$\begin{aligned}
\left[ \frac{\partial^\kappa \tilde{c}_{m,n}(\vec{x})}{\partial x^\kappa} \right]_{\vec{x}=\vec{\Omega}} &= \left[ \frac{\partial^\kappa}{\partial x^\kappa} \left( \langle \tilde{\phi}_m | \tilde{\psi}_{\vec{x}} \rangle \langle \tilde{\psi}_{\vec{x}} | \tilde{\phi}_n \rangle \right) \right]_{\vec{x}=\vec{\Omega}} \\
&= \sum_{k=0}^{\kappa} \binom{\kappa}{k} \langle \tilde{\phi}_m | \partial_{x^{(k)}} \tilde{\psi}_{\vec{\Omega}} \rangle \langle \partial_{x^{(\kappa-k)}} \tilde{\psi}_{\vec{\Omega}} | \tilde{\phi}_n \rangle,
\end{aligned} \tag{52}$$

which can be evaluated using Eq. 30 by continuing the Gram-Schmidt procedure to find all the required matrix elements of  $W$ . It is clear from Eq. 51 that using the perturbation theory result of Eq. 34 will result in a QCE  $\xi_Q = O(\gamma^\kappa)$ . On the other hand, the CE for direct imaging can be analyzed using a generalization of the series expansion of Eq. (40). If  $f(\gamma) = f_0 + \sum_{n=\kappa}^{\infty} f_n \gamma^n$  and  $g(\gamma) = f_0 + \sum_{n=\kappa}^{\infty} g_n \gamma^n$ , then

$$\begin{aligned}
f(\gamma)^s g(\gamma)^{1-s} &= f_0 + \sum_{n=1}^{2\kappa} (s f_n + (1-s) g_n) \gamma^n \\
&\quad - \frac{1}{2f_0} s(1-s) (f_\kappa - g_\kappa)^2 \gamma^{2\kappa} \\
&\quad + O(\gamma^{2\kappa+1}).
\end{aligned} \tag{53}$$

Applying this series to the integral given by Eq. (36) along with Eq. (38), term-by-term integration of  $Q_s$  can be performed up to order  $\kappa - 1$  in  $\gamma$  using the identity in Eq. (42), resulting in  $Q_s = 1 + O(\gamma^{2\kappa})$  and  $\xi_{\text{C, Direct}} = O(\gamma^{2\kappa})$ . The scaling gap between the quantum limit and the CE for direct imaging is then at least of the order  $\gamma^\kappa$ .

In the opposite scenario, when the two objects have different first moments in  $x_{\text{obj}}$  or  $y_{\text{obj}}$  (i.e., different centroids), we encounter different behavior: the scaling gap between the quantum limit and direct imaging vanishes. For the quantum Chernoff exponent, the states  $\rho_j$  can be approximated using Eq. (51), with  $\kappa = 1$ . Since lateral shifts of the reference frame should not affect the quantum Chernoff exponent, it is valid to move the origin of the object plane coordinate system so that the Cartesian first moments of one of the two objects are zero, i.e.,  $m_{1,x_{\text{obj}}} = m_{1,y_{\text{obj}}} = 0$ . As a result, the state  $\rho_1 = |\phi_1\rangle\langle\phi_1| + O(\gamma^2)$  is a pure state up to first order in  $\gamma$ , and the QCE is given by  $\xi_Q = -\log[F(\rho_1, \rho_2)] + O(\gamma^2)$ . After the approximation  $\log(1+u) = u + O(u^2)$ , the QCE becomes

$$\begin{aligned}
\xi_Q &= \left( m_{2,x_{\text{obj}}} \left[ \frac{\partial \tilde{\Gamma}(\vec{x})}{\partial x} \right]_{\vec{x}=\vec{\Omega}} + m_{2,y_{\text{obj}}} \left[ \frac{\partial \tilde{\Gamma}(\vec{x})}{\partial y} \right]_{\vec{x}=\vec{\Omega}} \right) \gamma \\
&\quad + O(\gamma^2),
\end{aligned} \tag{54}$$

which is zero because  $\tilde{\Gamma}(\vec{x})$  is even in  $x$  and  $y$  for a circularly symmetric PSF. Therefore, the lowest nonzero order term of the QCE is still of order  $O(\gamma^2)$ . On the other hand, for the direct imaging Chernoff exponent, it is trivial to use Eq. (53) with  $\kappa = 1$  to find that

$\xi_{\text{C,Direct}} = O(\gamma^2)$  in the limit  $\gamma \ll 1$ , at least for zeroless PSFs. We therefore find that the scaling gap with

respect to  $\gamma$  between the QCE and the direct imaging CE disappears when the two objects have different centroids.